Monopole mining method for high-throughput screening for Weyl semimetals

Vsevolod Ivanov and Sergey Y. Savrasov
Department of Physics, University of California, Davis, California 95616, USA

(Received 22 October 2018; revised manuscript received 2 February 2019; published 18 March 2019)

Although topological invariants have been introduced to classify the appearance of protected electronic states at surfaces of insulators, there are no corresponding indices for Weyl semimetals whose nodal points may appear randomly in the bulk Brillouin zone (BZ). Here we use a well-known result that every Weyl point acts as a Dirac monopole and generates integer Berry flux to search for the monopoles on rectangular BZ grids that are commonly employed in self-consistent electronic structure calculations. The method resembles data mining technology of computer science and was demonstrated on locating the Weyl points in known Weyl semimetals. It was subsequently used in high-throughput screening of several hundreds of compounds and predicting a dozen materials hosting nodal Weyl points and/or lines.

DOI: 10.1103/PhysRevB.99.125124

I. INTRODUCTION

There has been recent surge of interest in topological quantum materials caused by the existence in these systems of robust electronic states insensitive to perturbations [1,2]. Z_2 invariants have been proposed to detect the protected (quantum-Hall–like) surface states in topological insulators (TIs) [3], and, for centrosymmetric crystals, this reduces to finding band parities of electronic wave functions at time-reversal invariant points in the Brillouin zone (BZ) [4]. For a general case, the calculation involves an integration of Berry fields [5], and has been implemented in numerical electronic structure calculations [6] with density functional theory. These methods have allowed for exhaustive searches to identify candidate materials hosting topological insulator phases [7–9].

Weyl semimetals (WSMs) are closely related systems characterized by a bulk band structure which is fully gapped except at isolated points described by the 2×2 Weyl Hamiltonian [2]. Sometimes these Weyl points extend into lines in the BZ, giving rise to nodal line semimetals (NLSMs) [10]. Due to their intriguing properties such as Fermi arc surface states [11], chiral anomaly induced negative magnetoresistance [12], and a semiquantized anomalous Hall effect [13,14], the search for WSM materials is currently very active. Unfortunately, their identification in the infinite space of chemically allowed compounds represents a challenge: there is no corresponding topological index characterizing WSM phase, and the Weyl points may appear randomly in the bulk BZ. General principles, such as broken time-reversal or inversion symmetry, or emergence of the WSM phase between topologically trivial and nontrivial insulating phases [11], are too vague to guide their high-throughput screening, and recent group theoretical arguments [15,16] to connect crystal symmetry with topological properties still await their practical realization. The progress in this field was mainly serendipitous, although the ideas based on band inversion mechanism [17] or analyzing mirror Chern numbers [18,19] were proven to be useful in many recent discoveries [20–24], and computer oriented searches of topological semimetals are beginning to appear [25–27].

In this work, we propose a straightforward method to identify Weyl semimetals by using a well-known result that every Weyl point acts as a Dirac monopole [28,29] producing a nonzero Berry flux when it is completely enclosed by a surface in the BZ. The enclosed charge is given by the chirality of the Weyl point, similar to the Gauss theorem in the Coulomb law. Rectangular grids of k points that are widely employed in self-consistent electronic structure calculations for the BZ integration, either via special points (Monkhorst-Pack) technique [30] or a tetrahedron method [31], are ideally suited for this purpose since they divide the volume of the BZ onto microcells and the electronic wave functions are automatically available at the corners of each microcell. It is thus a matter of rearranging the data to extract Berry phases of these wave functions in order to recover the Dirac monopoles inside the BZ. While there are some uncertainties connected to energy bands cutoffs used while defining Berry fields for metallic systems, our method allows a subsequent refinement provided a signal from a monopole is detected. The entire procedure resembles data mining technology in computer science as an intelligent method to discover patterns from large data sets in a (semi)automatic way so that the extracted data can subsequently be used in further analysis.

Since we are dealing with grids, there is a chance that the grid microcell will enclose both chiral positive and negative charges whose Berry fluxes cancel each other. Although resolution here is obviously adjustable by changing the grid size, and modern computers allow handling of thousands and even millions of k points in parallel, going for Weyl points that are too close makes no sense from both practical and fundamental reasons. Practically, properties such as anomalous Hall effect [13,14] are proportional to the distance between the Weyl points and so are the density of Fermi arc surface states [11]. Disorder, electronic interactions, thermal broadening, and the Heisenberg uncertainty principle provide fundamental limitations. Therefore, distances between the Weyl

points need not be smaller than a few percent of the reciprocal lattice spacing, and this does not require dealing with very dense grids.

Our paper is organized as follows. In Sec. II, we describe the monopole mining method and give tests by verifying locations of the Weyl points in several known systems, such as recently proposed TaAs [20,21] and CuF [24] Weyl semimetals. In Sec. III, we demonstrate how it can be used for high-throughput screening of WSMs by scanning several hundreds of compounds in the $p\bar{6}2m$ no. 189 space group with the ZrNiAl structure. We predict a dozen materials hosting WSM/NLSM behavior. Section IV is the conclusion.

II. METHOD

Here we outline the method to evaluate the Berry flux due to a single Weyl point that appears somewhere in the bulk BZ with its typical dispersion relationship $E(\mathbf{k}) = \pm v|\mathbf{k} - \mathbf{k}_{WP}|$ as illustrated in Fig. 1(a). We represent the BZ by reciprocal lattice translations $\mathbf{G}_{\nu=1,2,3}$ and divide it onto $N_1 \times N_2 \times N_3$ microcells. Each microcell is spanned by primitive vectors $\mathbf{q}_{\nu=1,2,3} = \mathbf{G}_\nu/N_\nu$ with its origin given by the grid of $\mathbf{k}$ points represented by three integers $n_\nu = 0$, $N_\nu - 1$ as $\mathbf{k} = n_1\mathbf{q}_1 + n_2\mathbf{q}_2 + n_3\mathbf{q}_3$.

The problem of finding the wave vector $\mathbf{k}_{WP}$ is reduced to recovering the microcell that contains the monopole. We define a link field that appears while evaluating the Berry phase using the finite difference method [6]:

$$U_{\mathbf{q}}(\mathbf{k}) = \frac{\det[\langle \mathbf{k}+\mathbf{q}j'|e^{i\mathbf{qr}}|\mathbf{k}j\rangle]}{|\det[\langle \mathbf{k}+\mathbf{q}j'|e^{i\mathbf{qr}}|\mathbf{k}j\rangle]|}. \quad (1)$$

Here the matrix elements between the periodic parts of the wave functions are cast into the form $\langle \mathbf{k}+\mathbf{q}j'|e^{i\mathbf{qr}}|\mathbf{k}j\rangle$, which frequently appear in density functional linear response calculations [32] and thus are straightforward to evaluate. The set of energy bands j is spanned over occupied states and includes those that cross the Fermi level. However, some uncertainty exists in this enumeration procedure because the Berry flux from the negative and positive branches of the monopole [bands 1 and 2 for the example shown in Fig. 1(a)] will cancel each other. For the example being discussed, this means that either band 1 or 2 (but not both) needs to be taken into account while evaluating Eq. (1). In real materials, this may result in contribution for some monopoles canceling, but since we are mostly interested in the Weyl points in the immediate vicinity of the Fermi level, varying the upper cutoff value for j by 1 or 2 will resolve this problem. We also note that the link field $U_{\mathbf{q}}(\mathbf{k})$ needs to be computed for the entire grid of k points, where the group symmetry operations help to generate the wave functions that are normally available within only irreducible portion of the BZ.

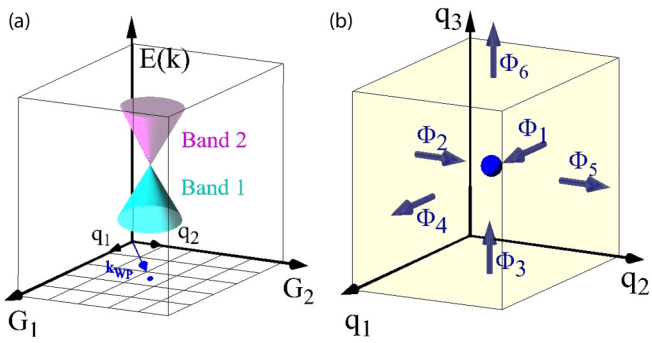

FIG. 1. (a) A typical cone dispersion relationship $E(\mathbf{k}) = \pm v|\mathbf{k} - \mathbf{k}_{WP}|$ for the Weyl point plotted within a rectangular area in k space set by divisions of reciprocal lattice translations $\mathbf{G}_1$ and $\mathbf{G}_2$ for a fixed value along the third translation $\mathbf{G}_3$. (b) The Weyl point located within a microcell set by the grid vectors $\mathbf{q}_1, \mathbf{q}_2, \mathbf{q}_3$ generates a Berry flux through each plaquette as given by the (right handed) circulation of the Berry connection with sign convention defined in text.

We now evaluate the Berry flux through faces of each microcell of the $N_1 \times N_2 \times N_3$ grid. This is illustrated in Fig. 1(b), where the flux $\Phi_{i=1,\ldots,6}$ through each plaquette with the origin at particular $\mathbf{k}$ and spanned by a pair of vectors $q_\mu q_\nu$ is conveniently encoded into the following formula:

$$2\pi\Phi \equiv \mathrm{Im}\ln\left[\frac{U_{\mathbf{q}_\mu}(\mathbf{k})U_{\mathbf{q}_\nu}(\mathbf{k}+\mathbf{q}_\mu)}{U_{\mathbf{q}_\nu}(\mathbf{k})U_{\mathbf{q}_\mu}(\mathbf{k}+\mathbf{q}_\nu)}\right]. \quad (2)$$

This procedure is similar to one employed while evaluating Z_2 invariants [6] on six two-dimensional tori introduced in Ref. [33], but now the roles of the tori are played by the slices of the BZ spanned by each pair of the reciprocal vectors $G_\mu G_\nu$ with a fixed value along the third vector G_ξ. We only need to take care of the fact that the flux as given by Eq. (2) produces right (alternatively left) handed circulation of the Berry connection, but the inner (or outer) normal should be chosen consistently for the total flux through each surface of the microcell. Thus, the total Berry flux is given by

$$c = \Phi_1 + \Phi_2 + \Phi_3 - \Phi_4 - \Phi_5 - \Phi_6. \quad (3)$$

Although the flux through each plaquette is generally non-integer, the total flux is guaranteed to be an integer since individual contributions (2) from adjacent plaquettes cancel each other in Eq. (3), up to an addition of $2\pi n$. Therefore c returns ether the chiral charge of the monopole or zero.

The entire algorithm is now viewed as an automated procedure that is either done following the self-consistent band structure calculation or "on the fly." We illustrate it on the example of TaAs Weyl semimetal whose electronic properties are well documented in recent literature [21]. We use a full potential linear muffin-tin orbital method (FP LMTO) developed by one of us [34] and perform a self-consistent density functional calculation with spin-orbit coupling using the generalized gradient approximation [35]. We subsequently set up a k grid using $20 \times 20 \times 20$ divisions of the reciprocal lattice unit cell. These types of grids were previously shown to be sufficient in calculating Z_2 invariants in topological insulators [36]. For evaluating the link field, Eq. (1), the energy window is chosen to span the entire valence band with the cutoff value corresponding to the band number that crosses the Fermi level. It appears this is sufficient to recover all monopoles. The net result is that 24 out 8000 microcells produce nonzero Berry flux and give their approximate positions. We take the coordinates of the corresponding microcells (only microcells that are nonequivalent by symmetry are needed; two for TaAs) and mine these areas of k space by introducing similar rectangular grids inside each microcell in order to

refine the locations of the Weyl points to the positions (0.009, 0.506,0) and (0.019, 0.281, 0.579) in units $2\pi/a$, $2\pi/a$, $2\pi/c$. This is in agreement with the previous calculation [21].

We also considered CuF, recently predicted to be a Weyl semimetal by one of us [24]. The exact same setup ($20 \times 20 \times 20$ divisions with the energy panel spanned till the band that crosses the Fermi level) returns 24 microcells that are all related by symmetry. Zooming into one microcell returns the following location of the Weyl point: $(0.281, 0.119, 0)2\pi/a$, consistent with our previous result [24].

III. RESULTS

To demonstrate the predictive power of the method, we scanned several hundreds noncentrosymmetric hexagonal compounds in the $p\bar{6}2m$ (no. 189) space group with ZrNiAl structure (see Fig. 2). Their complete crystallographic data can be found in Ref. [37]. Topological electronic structures in few of these systems have already drawn recent attention. CaAgP was predicted to be a line-node Dirac semimetal while CaAgAs was found to be a strong topological insulator [38]. Similar properties have been discussed for NaBaBi under pressure [39]. We perform self-consistent band structure calculations and the subsequent monopole mining procedure in exactly the same manner as we illustrated for TaAs and CuF. The experimental lattice constants from Ref. [37] have been utilized while the discrepancies brought by the differences in utilizing theoretically predicted lattice parameters were found to be small.

As many of the compounds in this structure include rare earth elements with their f electron states appearing in the vicinity of the Fermi level, we first provide a list of only those compounds that do not explicitly include lanthanides (see Table I). These are the systems for which density functional based calculations can be trusted in general. Quite a few of them include magnetic elements (such as Fe) which can potentially develop a magnetic order at low temperatures. Unfortunately, the literature contains very limited information about the existence of magnetism and the type of order (ferro, antiferro, incommensurate, etc.), and, due to the absence of established theoretical procedures to search for the lowest energy ground state in the infinite space of possible magnetic configurations, all calculations reported here assume a paramagnetic ground state.

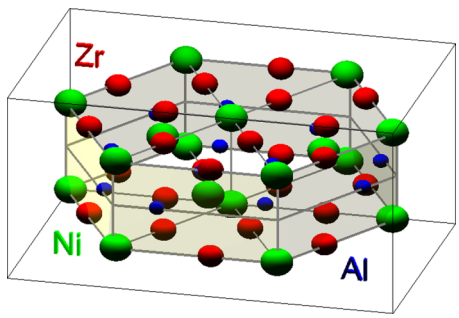

FIG. 2. ZrNiAl-type crystal structure (no. 189 space group $p\bar{6}2m$) of noncentrosymmetric hexagonal compounds studied in this work.

TABLE I. List of noncentrosymmetric hexagonal compounds in the $p\bar{6}2m$ (no. 189) space group with the ZrNiAl structure studied in this work. The compounds containing a lanthanide element are explicitly excluded from the table.

Class	$X =$	Class	$X =$
CrAsX	Ti, Pd, Fe, Co, Ni, Rh	XPtIn	Sc, Y
MnAsX	Ti, Ni, Rh, Fe, Pd, Ru	TiGeX	Co, Pd
ScGeX	Fe, Rh, Cu, Os, Pd, Ru	ZrCoX	Ga, Sn
XSiRe	Hf, Ta, Ti, Zr	ZrGeX	Os, Zn
HfGeX	Fe, Os, Rh, Ru	XNiGa	Hf, Zr
FeAsX	Ti, Co, V, Ni	ScPX	Ir, Na
XPNi	Fe, Mo, W, Co	MnGeX	Pd, Rh
XGeMn	Hf, Nb, Sc, Ta	CrPX	Pd, Ni
TiPX	Cr, Os, Ru	HfXRu	P, As
ZrPX	Os, Mo, Ru	XAsOs	Hf, Zr
MnPX	Rh, Pd, Ni	XPdPb	Ca, Y
ScSiX	Cu, Ru, Mn	XSiMn	Nb, Ta
CaXCd	Ge, Sn, Pb	HfSiX	Os, Ru
XAsPd	Hf, Ti, Zr	CaXAg	P, As
XNiAl	Hf, Y, Zr	ZrXRu	Si, As
XBFe	Nb, Ta	NbCrX	Ge, Si

Other: YRhSn, YAuCd, YPdMg, YNiIn, ScGeAg
YPdAl, YInMg, YAuZn, YPbAg, YPdTl
YAuMg, YPdZn, YPdTl, YSiAg, YRhIn
YTlMg, YAgMg, YAuIn, YCuIn, YGaMg
HfIrSn, YPdIn, YCuAl, YGeLi, YPtSn
YCuMg, BaBiNa, YAlMg, ScSnAg, YSiLi

We can also comment on the compounds that include lanthanide elements. They can be separated into two large groups. The first group includes the materials where the narrow f band appears crossing the Fermi level in the calculated band structures. This would be an indication that a many-body renormalization of the single-particle spectra (such as band narrowing, multiplet transitions, etc.) is expected. Although modern electronic structure approaches based on combinations of density functional and dynamical mean field theories [40] allow handling such cases, those are outside the scope of the present study, and we do not study topological properties of these compounds. The second group includes the materials with either a fully empty or fully occupied f band, namely f^0: LaAuCd, LaAuIn, LaAuMg, LaCuIn, LaCuMg, LaInMg, LaIrSn, LaNiIn, LaNiZn, LaPdCd, LaPdHg, LaPdIn, LaPdMg, LaPdPb, LaPdSn, LaPdTl, LaPtIn, LaPtPb, LaPtSn, LaRhIn, LaRhSn, LaTlMg; f^{14}: LuAsPd, LuAuIn, LuAuZn, LuCuIn, LuGaMg LuGeAg, LuGeLi, LuInMg, LuIrSn, LuNiAl LuNiIn, LuNiPb, LuPbAg, LuPdIn, LuPdSn LuPdZn, LuPtIn, LuPtSn, LuRhSn, LuSiAg, LuTlMg. These are the cases where the static mean field description can in principle capture single-particle excitations (apart from the question of whether the position of the f band is correctly predicted by such theory).

There are a few materials that include Sm ion with its nonmagnetic configuration f^6: SmAgMg, SmAuCd, SmAuIn, SmAuMg, SmCuAl, SmCuIn, SmIrIn, SmIrSn, SmNiAl, SmNiIn, SmNiSn, SmNiZn, SmPdCd, SmPdHg, SmPdIn, SmPdMg, SmPdPb, SmPdTl, SmPtIn, SmPtMg, SmPtPb, SmPtSn, SmRhIn, SmRhSn, SmSiAg, SmTlMg. Here

TABLE II. List of nonequivalent Weyl and triple points (in units $2\pi/a$, $2\pi/a$, $2\pi/c$), their numbers, and energies relative to the Fermi level (in eV) recovered using the monopole mining method for noncentrosymmetric hexagonal compounds in the $p\bar{6}2m$ (no. 189) space group with the ZrNiAl structure that are predicted to exhibit Weyl/nodal-line semimetal behavior. The typical appearance of the Weyl points in the Brillouin zone is indicated as either sort A or B, as illustrated in Figs. 3(a) and 3(b).

Comp.	Topological Points	Sort	No.	E (eV)
LaInMg	(0.00000, 0.36868,0.01123)	Weyl-A	12	−0.06
LuGeAg	(0.00000, 0.42190,0.00098)	Weyl-A	12	−0.23
YGeLi	(0.00000, 0.27793,0.00817)	Weyl-A	12	−0.13
YPbAg	(0.00000, 0.40335,0.03142)	Weyl-A	12	−0.09
YSiAg	(0.00000, 0.37864,0.00384)	Weyl-A	12	−0.09
HfPRu	(0.46280, 0.06931,0.0221)	Weyl-B	24	+0.06
ZrPRu	(0.45982, 0.07532,0.01698)	Weyl-B	24	+0.06
LaTlMg	(0.00000, 0.38916, 0.03236)	Weyl-A	12	−0.13
	(0.41450, 0.02567, 0.00724)	Weyl-B	24	−0.13
YTlMg	(0.00000, 0.43303, 0.02319)	Weyl-A	12	−0.05
	(0.44076, 0.02908, 0.00441)	Weyl-B	24	−0.11
LuAsPd	(0.00000, 0.11481, 0.14140)	Weyl-A	12	+0.18
	(0.00000, 0.12004, 0.13942)	Weyl-A	12	+0.19
ZrAsOs	(0.47365, 0.02591, 0.04792)	Weyl-B	24	+0.02
	0.47406, 0.01215, 0.04789	Weyl-B	24	+0.02
TiGePd	(0.00000, 0.00000, 0.16495)	Triple	2	+0.14
	(0.00000, 0.00000, 0.20775)	Triple	2	+0.22
VAsFe	(0.00000, 0.000000, 0.32279)	Triple	2	+0.14
	(0.00000, 0.000000, 0.47625)	Triple	2	+0.19
	(0.00000, 0.38339, 0.17269)	Weyl-A	12	+0.09

$j = 5/2$ and $j = 7/2$ subbands appear below and above the Fermi level, respectively. The Coulomb renormalzation in these compounds has a predictable effect by renormalizing the spin-orbit coupling by the Hubard-type interaction, and the states in the immidiate vicinity of the Fermi level are not affected.

Out of the compounds that we studied, we clearly identify 11 materials which show WSM behavior, 1 NLSM, and 1 hosting both Weyl points and nodal lines. The two NLSMs also host topologically distinct triple fermion points [41]. Table II summarizes our results for each compound, giving the locations of the nonequivalent low-energy Weyl and/or triple points, their numbers, and relative energies E_F in eV. The Weyl points are generally viewed as type II according to the classification introduced in Ref. [42]. (Complete crystallographic and electronic structure data for these compounds is given in the Supplemental Material [43].)

Many of the Weyl semimetals that we predict in our work display remarkably similar locations of their Weyl points. LaInMg [44], LuGeAg [45], YGeLi [46], YPbAg [47], and YSiAg [48] exhibit 6 pairs (chiral positive and negative) of points, that are all symmetry related and are only slightly displaced from the $k_z = 0$ plane. They are located along the ΓM direction in the BZ. We illustrate their precise positions for LaInMg in Fig. 3(a) and refer to them in Table II as Weyl points of sort A. We find that HfPRu [49], and ZrPRu [44] show another sort (referred to as sort B) of Weyl points, namely 12 pairs that are shifted symmetrically away from the ΓK line [see Fig. 3(b)]. Interestingly, a similar behavior is seen for LaTlMg [50] and YTlMg [44] which show both sorts (A and B) of Weyl points. LuAsPd [51] shows two kinds of sort A Weyl points (24 total), while ZrAsOs [52] shows two kinds of sort B Weyl points (48 total). Their displacement from $k_z = 0$ plane is much larger than the one found in previous cases. For each reported Weyl point, we also provide independent verification by calculating the band structures along k_x, k_y and k_z directions with the boundary vectors confining the Weyl point. These data can be found in the Supplemental Material [43].

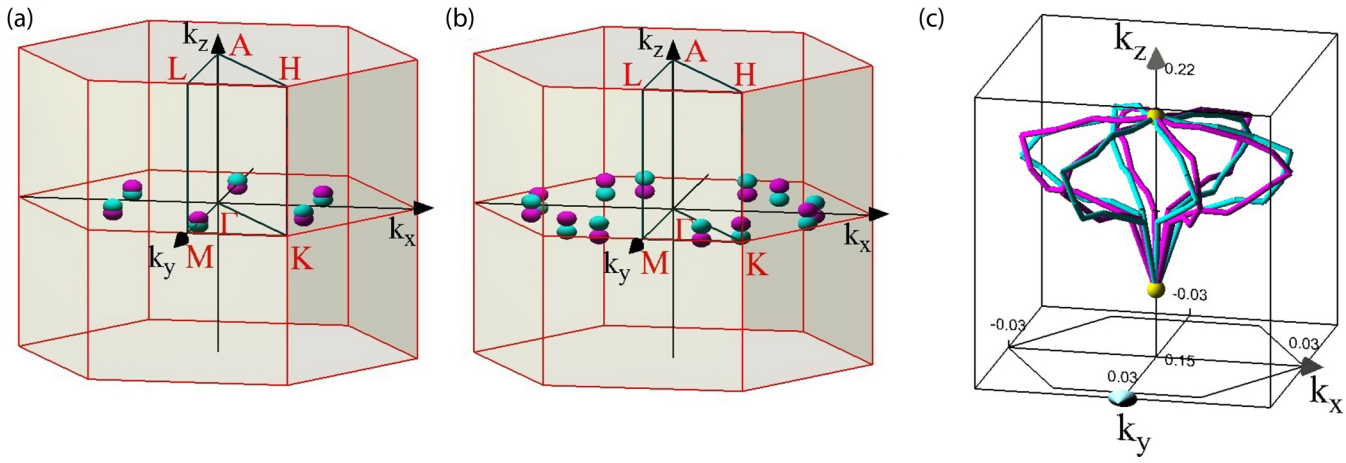

FIG. 3. (a) Positions of 6 pairs (cyan for chiral positive and magenta for chiral negative) of low-energy Weyl points seen along the ΓM direction in the BZ for LaInMg and referenced in Table II as sort A; (b) Positions of 12 pairs of Weyl points that are shifted symmetrically away from the ΓK line for HfPRu and referenced in Table II as sort B; (c) A set of nodal lines for TiGePd that is recovered by the monopole mining method presented in this work. The color (cyan and magenta) distinguishes chiral positive and negative lines, respectively. The zoomed area of the BZ is bounded by $0.15 \leqslant 2\pi k_z/c \leqslant 0.22$ and $-0.03 \leqslant 2\pi k_{x,y}/a \leqslant +0.03$. Also shown in yellow are the triple degenerate topological points [41].

Another interesting outcome of our high-throughput screening is the materials exhibiting nodal lines and triple-point fermions. TiGePd [53] and VAsFe [54] both host 12 pairs (chiral positive and negative) of nodal lines that are located very close to the ΓA direction in the BZ. We illustrate this behavior for TiGePd in Fig. 3(c) by zooming into the area of the BZ bounded by $0.15 \leqslant 2\pi k_z/c \leqslant 0.22$ and $-0.03 \leqslant 2\pi k_{x,y}/a \leqslant +0.03$. Interestingly, the nodal lines start and end at triple degenerate points that have recently enriched our classification of the topological objects [41]. These triple points are located at the ΓA line of the BZ. We provide their coordinates for TiGePd and VAsFe in Table II.

One of the most striking features of Weyl semimetals is the presence of the Fermi arcs in their one-electron surface spectra [11]. Although computations of their shapes are possible via a self-consistent supercell (slab) calculation of the surface energy bands, given the number of compounds that we deal in this work, it is a computationally demanding study. Nevertheless, since the arcs connect the Weyl points of different chirality, one can expect that most of the materials that we list in Table II would have rather short arcs since the distances between positive and negative chiral charges are quite small. One notable exception is VAsFe which, as we list in Table II, exhibits not only nodal lines and triple points, but also a set of Weyl points which are well separated from each other. These are expected to produce very long Fermi arcs for the (100) or (110) crystallographic types of surfaces. One can also expect that their contribution to the anomalous Hall coefficient should be large since the latter is known to be directly proportional to the distance between the Weyl points [13]. We have recently shown [55] that long and straight Fermi arcs are generally capable of supporting nearly dissipationless surface currents, therefore it could be interesting to explore such a possibility in VAsFe.

IV. CONCLUSION

In conclusion, we presented an automated monopole mining method to identify Weyl and nodal-line semimetals. We tested the method by recovering the Weyl points in several known systems as well as demonstrating its predictive power by high-throughput screening of hundreds noncentrosymmetric hexagonal compounds in the $p\bar{6}2m$ (no. 189) space group and finding 13 materials whose locations of the topological nodal points and lines have been reported. As we judge from our calculated energy bands, the WSMs identified in this work exhibit regular Fermi surface states while the Weyl points are not exactly pinned at the Fermi level. This is similar to other recently discovered WSMs, such as TaAs [21], for which experimental studies of large negative magnetoresistance were recently performed [56]. Despite the latter representing a signature of the much celebrated chiral anomaly feature in Weyl semimetals, there exists an obvious problem of distinguishing contributions from the Weyl points and regular Fermi states. In this regard our automated approach should be helpful for scanning vast material databases in identifying an ideal WSM with only nodal points at the Fermi level, as originally envisioned in pyrochlore iridates [11].

ACKNOWLEDGMENTS

The work was supported by NSF DMR Grant No. 1411336.

[1] For a review, see, e.g., M. Z. Hasan and C. L. Kane, Colloquium: Topological insulators, Rev. Mod. Phys. **82**, 3045 (2010).
[2] For a review, see, e.g., N. P. Armitage, E. J. Mele, and A. Vishwanath, Weyl and Dirac semimetals in three-dimensional solids, Rev. Mod. Phys. **90**, 015001 (2018).
[3] C. L. Kane and E. J. Mele, Z_2 Topological Order and the Quantum Spin Hall Effect, Phys. Rev. Lett. **95**, 226801 (2005).
[4] L. Fu and C. L. Kane, Topological insulators with inversion symmetry, Phys. Rev. B **76**, 045302 (2007).
[5] L. Fu and C. L. Kane, Time reversal polarization and a Z_2 adiabatic spin pump, Phys. Rev. B **74**, 195312 (2006).
[6] T. Fukui and Y. Hatsugai, Quantum spin Hall effect in three dimensional materials: Lattice computation of Z_2 topological invariants and its Application to Bi and Sb, J. Phys. Soc. Jpn. **76**, 053702 (2007).
[7] H. Lin, L. A. Wray, Y. Xia, S. Xu, S. Jia, R. J. Cava, A. Bansil, and M. Z. Hasan, Half-Heusler ternary compounds as new multifunctional experimental platforms for topological quantum phenomena, Nat. Mater. **9**, 546 (2010).
[8] S. Chadov, X. Qi, J. Kubler, G. H. Fecher, C. Felser, and S. C. Zhang, Tunable multifunctional topological insulators in ternary Heusler compounds, Nat. Mater. **9**, 541 (2010).
[9] M. G. Vergniory, L. Elcoro, C. Felser, B. A. Bernevig, and Z. Wang, A complete catalogue of high-quality topological materials, Nature (London) **566**, 480 (2019).
[10] A. A. Burkov, M. D. Hook, and L. Balents, Topological nodal semimetals, Phys. Rev. B **84**, 235126 (2011).
[11] X. Wan, A. M. Turner, A. Vishwanath, and S. Y. Savrasov, Topological semimetal and Fermi-arc surface states in the electronic structure of pyrochlore iridates, Phys. Rev. B **83**, 205101 (2011).
[12] H. B. Nielsen and M. Ninomiya, The Adler-Bell-Jackiw anomaly and Weyl fermions in a crystal, Phys. Lett. B **130**, 389 (1983).
[13] K.-Yu. Yang, Y.-M. Lu, and Y. Ran, Quantum Hall effects in a Weyl semimetal: Possible application in pyrochlore iridates, Phys. Rev. B **84**, 075129 (2011).
[14] A. A. Burkov and L. Balents, Weyl Semimetal in a Topological Insulator Multilayer, Phys. Rev. Lett. **107**, 127205 (2011).
[15] H. C. Po, A. Vishwanath, and H. Watanabe, Symmetry based indicators of band topology in the 230 space groups, Nat. Commun. **8**, 50 (2017).
[16] J. Krutho, J. de Boer, J. van Wezel, C. L. Kane, and R.-J. Slager, Topological Classification of Crystalline Insulators

through Band Structure Combinatorics, Phys. Rev. X **7**, 041069 (2017).

[17] B. A. Bernevig, T. L. Hughes, and S.-C. Zhang, Quantum spin Hall effect and topological phase transition in HgTe quantum wells, Science **314**, 1757 (2006).

[18] T. H. Hsieh, H. Lin, J. Liu, W. Duan, A. Bansil, and L. Fu, Topological crystalline insulators in the SnTe material class, Nat. Commun. **3**, 982 (2012).

[19] H. Weng, J. Zhao, Z. Wang, Z. Fang, and X. Dai, Topological Crystalline Kondo Insulator in Mixed Valence Ytterbium Borides, Phys. Rev. Lett. **112**, 016403 (2014).

[20] S.-Y. Xu, I. Belopolski, N. Alidoust, M. Neupane, G. Bian, C. Zhang, R. Sankar, G. Chang, Z. Yuan, C.-C. Lee, S.-M. Huang, H. Zheng, J. Ma, D. S. Sanchez, B. K. Wang, A. Bansil, F. Chou, P. P. Shibayev, H. Lin, S. Jia, and M. Z. Hasan, Discovery of a Weyl fermion semimetal and topological Fermi arcs, Science **349**, 613 (2015).

[21] B. Q. Lv, H. M. Weng, B. B. Fu, X. P. Wang, H. Miao, J. Ma, P. Richard, X. C. Huang, L. X. Zhao, G. F. Chen, Z. Fang, X. Dai, T. Qian, and H. Ding, Experimental Discovery of Weyl Semimetal TaAs, Phys. Rev. X **5**, 031013 (2015).

[22] L. Huang, T. M. McCormick, M. Ochi, Z. Zhao, M.-T. Suzuki, R. Arita, Y. Wu, D. Mou, H. Cao, J. Yan, N. Trivedi, and A. Kaminski, Spectroscopic evidence for a type II Weyl semimetallic state in $MoTe_2$, Nat. Mater. **15**, 1155 (2016).

[23] G. Chang, S.-Y. Xu, D. S. Sanchez, S.-M. Huang, C.-C. Lee, T.-R. Chang, G. Bian, H. Zheng, I. Belopolski, N. Alidoust, H.-T. Jeng, A. Bansil, H. Lin, and M. Z. Hasan, A strongly robust type II Weyl fermion semimetal state in Ta_3S_2, Sci. Adv. **2**, e1600295 (2016).

[24] Y. Du, E.-J. Kan, H. Xu, S. Y. Savrasov, and X. Wan, Turning copper metal into Weyl semimetal, Phys. Rev. B **97**, 245104 (2018).

[25] D. Gresch, G. Autes, O. V. Yazyev, M. Troyer, D. Vanderbilt, B. A. Bernevig, and A. A. Soluyanov, Z2Pack: Numerical implementation of hybrid Wannier centers for identifying topological materials, Phys. Rev. B **95**, 075146 (2017).

[26] T. Zhang, Y. Jiang, Z. Song, H. Huang, Y. He, Z. Fang, H. Weng, and C. Fang, Catalogue of topological electronic materials, Nature (London) **566**, 475 (2019).

[27] F. Tang, H.-C. Po, A. Vishwanath, and X. Wan, Towards ideal topological materials: Comprehensive database searches using symmetry indicators, Nature (London) **566**, 486 (2019).

[28] G. E. Volovik, Zeros in the fermion spectrum in superfluid systems as diabolical points, Pis'ma Zh. Eksp. Teor. Fiz. **46**, 81 (1987) [Sov. Phys. JETP Lett. **46**, 99 (1987)].

[29] Z. Fang, N. Nagaosa, K. S. Takahashi, A. Asamitsu, R. Mathieu, T. Ogasawara, H. Yamada, M. Kawasaki, Y. Tokura, and K. Terakura, The anomalous Hall effect and magnetic monopoles in momentum space, Science **302**, 92 (2003).

[30] H. J. Monkhorst and J. D. Pack, Special points for Brillonin-zone integrations, Phys. Rev. B **13**, 5188 (1976).

[31] O. Jepsen and O. K. Andersen, No error in the tetrahedron integration scheme, Phys. Rev. B **29**, 5965 (1984).

[32] S. Y. Savrasov, Linear-response Calculations of Lattice Dynamics Using Muffin-tin Basis Cets, Phys. Rev. Lett. **69**, 2819 (1992).

[33] J. E. Moore and L. Balents, Topological invariants of time-reversal-invariant band structures, Phys. Rev. B **75**, 121306 (2007).

[34] S. Y. Savrasov, Linear-response theory and lattice dynamics: A muffin-tin-orbital approach, Phys. Rev. B **54**, 16470 (1996).

[35] J. P. Perdew, K. Burke, and M. Ernzerhof, Generalized Gradient Approximation Made Simple, Phys. Rev. Lett. **77**, 3865 (1996).

[36] W. Fenga, J. Wend, J. Zhoua, D. Xiao, and Y. Yao, First-principles calculation of Z_2 topological invariants within the FP-LAPW formalism, Comput. Phys. Commun. **183**, 1849 (2012).

[37] *Handbook of Inorganic Substance*s, edited by P. Villars, K. Cenzual, and R. Gladyshevskii (De Gruyter, Berlin, 2015).

[38] A. Yamakage, Y. Yamakawa, Y. Tanaka, and Y. Okamoto, Line-node Dirac semimetal and topological insulating phase in noncentrosymmetric pnictides CaAgX (X = P, As), J. Phys. Soc. Jpn. **85**, 013708 (2016).

[39] Y. Sun, Q.-Z. Wang, S.-C. Wu, C. Felser, C.-X. Liu, and B. Yan, Pressure-induced topological insulator in NaBaBi with right-handed surface spin texture, Phys. Rev. B **93**, 205303 (2016).

[40] G. Kotliar, S. Y. Savrasov, K. Haule, V. S. Oudovenko, O. Parcollet, and C. A. Marianetti, Electronic structure calculations with dynamical mean-field theory, Rev. Mod. Phys. **78**, 865 (2006).

[41] Z. Zhu, G. W. Winkler, Q.-S. Wu, J. Li, and A. A. Soluyanov, Triple Point Topological Metals, Phys. Rev. X **6**, 031003 (2016).

[42] A. A. Soluyanov, D. Gresch, Z. Wang, Q. Wu, M. Troyer, X. Dai, and B. A. Bernevig, Type-II Weyl semimetals, Nature (London) **527**, 495 (2015).

[43] See Supplemental Material at http://link.aps.org/supplemental/10.1103/PhysRevB.99.125124 for complete data for the topological materials predicted in this work: the band structures near the Fermi level, energy panels used for defining the Berry connection, positions of low-energy topological nodal points in the Brillouin zone, as well as energy band dispersions in the vicinity of the nodal points.

[44] R. Kraft, M. Valldor, D. Kurowski, R.-D. Hoffmann, and R. Poettgen, Ternary indides REMgIn (RE = Y, La-Nd, Sm, Gd-Tm, Lu): Synthesis, structure and magnetic properties, Z. Naturforsch. **59b**, 513 (2004).

[45] B. Gibson, R. Pöttgen, R. K. Kremer, A. Simon, and K. R. A. Ziebeck, Ternary germanides LnAgGe (Ln = Y, Sm, Gd, Lu) with ordered Fe_2P-type structure, J. Alloys Compd. **239**, 34 (1996).

[46] A. Czybulka, G. Steinberg, and H.-U. Schuster, Darstellung und Struktur ternärer Silizide und Germanide des Lithiums mit den Seltenen Erden Y und Gd im Fe_2P-Typ, Z. Naturforsch. **34b**, 1057 (1979).

[47] L. D. Gulay, Crystal structure of RAgPb (R5Y, Er, Tm, Lu) compounds, J. Alloys Compd. **314**, 219 (2001).

[48] I. Savysyuk, O. Shcherban, N. Semuso, R. Gladyshevskii, and E. Gladyshevskii, The {Y, Pr}–Ag–Si systems: Isothermal sections and crystal structures, Chem. Met. Alloys **5**, 103 (2012).

[49] G. P. Meisner and H. C. Ku, The superconductivity and structure of equiatomic ternary transition metal pnictides, Appl. Phys. A **31**, 201 (1983).

[50] R. Kraft and R. Poettgen, Ternary thallides REMgTl (RE = Y, La-Nd, Sm, Gd-Tm, Lu), Z. Naturforsch. **60b**, 265 (2005).

[51] D. Johrendt and A. Mewis, Darstellung und Kristallstrulauren der Verbindungen SEPdAs (SE = La-Lu), J. Alloys Compd. **183**, 210 (1992).

[52] G. P. Meisner, H. C. Eu, and H. Barz, Superconducting equiatomic ternanry transition metal arsenides, Mater. Res. Bull. **18**, 983 (1983).

[53] R. Demchyna, Y. Prots, and U. Schwarz, Crystal structures of titanium palladium germanium, TiPdGe, *two polymorphic modifications*, Z. Kristallogr. NCS **222**, 173 (2007).

[54] M. Roy-Montreuil, B. Deyris, A. Michel, A. Rouault, P. l'Heritier, A. Nylund, J. P. Senateur, and R. Fruchart, Nouuveax composes ternaires MM'P et MM'As, interactions metalliques et structures, Mater. Res. Bull. **7**, 813 (1972).

[55] G. Resta, S.-T. Pi, X. Wan, and S. Y. Savrasov, High surface conductivity of Fermi-arc electrons in Weyl semimetals, Phys. Rev. B **97**, 085142 (2018).

[56] X. Huang, L. Zhao, Y. Long, P. Wang, D. Chen, Z. Yang, H. Liang, M. Xue, H. Weng, Z. Fang, X. Dai, and G. Chen, Observation of the Chiral-Anomaly-Induced Negative Magnetoresistance in 3D Weyl Semimetal TaAs, Phys. Rev. X **5**, 031023 (2015).